


Quantum Theory of Longitudinal-Transverse Polaritons in Nonlocal Thin Films

Christopher R. Gubbin^{*} and Simone De Liberato

School of Physics and Astronomy, University of Southampton, Southampton SO17 1BJ, United Kingdom

 (Received 25 August 2021; revised 29 October 2021; accepted 24 December 2021; published 27 January 2022)

When midinfrared light interacts with nanoscale polar dielectric structures, optical phonon propagation cannot be ignored, leading to a rich nonlocal phenomenology that we have only recently started to uncover. In properly crafted nanodevices this includes the creation of polaritonic excitations with hybrid longitudinal-transverse nature, which are predicted to allow energy funneling from longitudinal electrical currents to far-field transverse radiation. In this work we study the physics of these longitudinal-transverse polaritons in a dielectric nanolayer in which the nonlocality strongly couples epsilon-near-zero modes to longitudinal phonons. After having calculated the system's spectrum solving Maxwell's equations, we develop an analytical polaritonic theory able to transparently quantify the nonlocality-mediated coupling as a function of the system parameters. Such a theory provides a powerful tool for the study of longitudinal-transverse polariton interactions and we use it to determine the conditions required for the hybrid modes to appear.

DOI: [10.1103/PhysRevApplied.17.014037](https://doi.org/10.1103/PhysRevApplied.17.014037)

Photonic energy can be confined to deep subdiffraction length scales by hybridization of light with optically active transitions [1], thus storing part of the electromagnetic energy in the charges' kinetic energy [2]. In the midinfrared region this can be achieved by coupling light with the transverse optical phonons of a polar nanostructure, yielding hybrid light-matter excitations termed surface phonon polaritons (SPhPs) [3–5]. These modes are highly tuneable [6–10] and have broad applications in nonlinear optics [11–13], near-field imaging [14,15], design of midinfrared emitters [16], and fabrication of nanophotonic circuitry [17–19].

Because of their narrow linewidths and large field confinement, SPhPs can be strongly coupled to a variety of other resonances present in nanostructured devices. Polaritonic excitations resulting from such strong coupling are hybrid quasiparticles whose unique properties can be understood as admixtures of those of their bare components. Resonances that have been experimentally demonstrated to be strongly coupled with SPhPs include localized phonon polaritons [20], epsilon-near-zero (ENZ) modes [21], weak phonon excitations [22], and, more recently, vibrational transitions in organic molecules [23].

Of particular relevance for the present work, in Ref. [22] SPhPs localized in silicon carbide (SiC) nanopillars were demonstrated to be strongly coupled to longitudinal optical (LO) phonons whose dispersion is folded along the c axis of the 4H-SiC polytype. The resulting excitations were named longitudinal-transverse polaritons (LTPs) because

they have the unusual feature of possessing both a longitudinal nature from their LO component, and a transverse one from their electromagnetic SPhP component. These recently observed LTP quasiparticles are an exciting system for applications in midinfrared optoelectronics, with a transverse photonic component able to radiate to the far field and a longitudinal matter component able to interact with electrical currents. They could aid development of efficient and low-cost midinfrared optoelectronic devices, not requiring the usual quantum cascade structures to convert electrical currents into midinfrared radiation [24]. Note that longitudinal-transverse strong coupling has recently also been observed in fluids [25].

As we showed in a series of recent papers [26–28], the coupling between longitudinal and transverse degrees of freedom can be more generally understood as a feature of nanoscopic polar devices where optical phonon propagation cannot be neglected. The usual local dielectric approximation then fails and the resulting nonlocal phenomenology driving the longitudinal-transverse coupling has important consequences on the performances of polar nanodevices, analogous to nonlocal effects in localized plasmons [29,30] and plasmon polaritons [31].

Polaritonic systems are usually studied using second quantized approaches [32–34], which were very successful in, e.g., the study of polariton-polariton [11,35] and electron-polariton [36,37] interactions. These are important for LTP systems; the former would allow for the description of exotic phonon polariton condensates, while the latter would be especially important for the development of phonon-polariton optoelectronics, allowing for

^{*}c.r.gubbin@soton.ac.uk

modeling of both the excitation of LTPs from electrical currents and their outcoupling to the far field. Extensions of the Hopfield polaritonic formalism to general nanophotonic devices, and even more to LTPs, becomes nevertheless problematic when the coupled resonances are morphology dependent. The bare uncoupled modes can then be difficult to identify or altogether ill-defined. In these cases only a holistic solution of the Maxwell equations coupled to spatially varying dielectrics could seem to provide a predictive description of the hybrid resonances, thus foregoing the explanatory and operational power of polaritonic formalism.

In this work we achieve two objectives that we consider timely and relevant to advance our understanding and modeling capabilities of solid-state midinfrared nanophotonic devices. (1) Using the approach we developed in Ref. [26], that is, solving the full system of Maxwell equations in the nonlocal dielectric and taking mechanical boundary conditions into account, we study the nonlocal physics of a thin nanolayer, in which LTPs are formed by the strong coupling of the layer's epsilon-near-zero resonance to the layer's discrete LO phonons. (2) We develop an analytical second-quantized polaritonic formalism, allowing us to describe the system in terms of coupled harmonic oscillators. The solution of the nonlocal problem then requires only the bare frequencies of the modes in the range of interest and their couplings. This is a powerful theoretical tool for nonlocal midinfrared nanophotonics, as it alleviates the complexity of the full nonlocal theory developed previously [26–28]. In this work, by focusing on a specific geometry, we demonstrate formal equivalence between the nonlocal theory describing SPhP-LO coupling mediated by the nonlocal boundary conditions and a simple multimode coupled linear theory. The parameters of such a theory, which we obtain in analytical form as functions of the geometric and material parameters of the sample, are useful tools for inverse design of nonlocal nanophotonic elements. Moreover, the polaritonic solution describes the system in terms of hybrid quasiparticles whose interactions can be studied with tested tools both below and above the lasing threshold [35]. It is thus a key tool for future studies of the LTP-mediated coupling between electrical currents and far-field midinfrared electromagnetic radiation.

A large number of technologically relevant polar nonlocal systems are expected to be created by atomic layer deposition, which allows for high-precision fabrication of nanometer-scale films along the growth direction [21,38,39], with structure perpendicular to the grown axis created by etching [20,40]. In these systems the thin film defines the phonon resonator, while the perpendicular structure defines the optical one. For that reason, in this paper we consider a simple representative system, whose photonic modes can be found analytically, the trilayer waveguide shown in Fig. 1. This consists of a polar film of thickness d and relative permittivity ϵ_2 sandwiched between identical

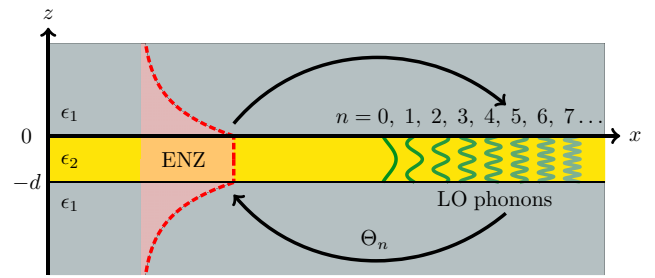


FIG. 1. The waveguide under study in this work. Illustrated are the out-of-plane electric field E_z for the ENZ mode (red) and localized phonons (green). The coupling frequency Θ_n couples the ENZ mode to the n th longitudinal phonon mode.

semi-infinite regions with identical relative permittivity ϵ_1 . The waveguide dispersion in the local response approximation can be derived considering TM polarized electromagnetic fields and applying electromagnetic boundary conditions on the components of the magnetic and electric fields parallel to the surface \mathbf{H}_{\parallel} and \mathbf{E}_{\parallel} [41,42], leading to the eigenequation (derived in Appendix A)

$$F = 2 - \tanh(\alpha_2 d) \left[\frac{\epsilon_2 \alpha_1}{\epsilon_1 \alpha_2} + \frac{\epsilon_1 \alpha_2}{\epsilon_2 \alpha_1} \right] = 0, \quad (1)$$

where $\alpha_i^2 = |\mathbf{k}|^2 - \epsilon_i \omega^2 / c^2$ is the out-of-plane wave vector in the i th layer and \mathbf{k} is the in-plane wave vector. We consider region 1 as a positive lossless dielectric, while region 2 is a dissipative polar dielectric characterized by a Lorentzian dielectric function [5]

$$\epsilon_2(\omega) = \epsilon_{\infty} \left[\frac{\omega_L^2 - \omega(\omega + i\gamma)}{\omega_T^2 - \omega(\omega + i\gamma)} \right], \quad (2)$$

where ω_L (ω_T) is the longitudinal (transverse) bulk optical phonon frequency, ϵ_{∞} is the high-frequency dielectric constant, and γ is the phonon loss rate, which, for the sake of simplicity, we consider frequency and polarization independent.

A thick polar film acts as a semi-infinite medium, supporting isolated SPhP modes on each interface. These modes exist within the Reststrahlen region $\omega_T < \omega < \omega_L$, where $\epsilon_2(\omega) < 0$, illustrated by the nonshaded spectral regions in Figs. 2(a) and 2(b). Their dispersion is shown by the purple solid curve. When the film thickness d is less than the skin depth, the SPhPs on each film interface hybridize into symmetric and antisymmetric modes. This is shown in Figs. 2(a) and 2(b), where we plot dispersion $|F^{-1}|$ for 50 and 5 nm 3C-SiC films, respectively, using parameters $\omega_T = 797.0 \text{ cm}^{-1}$, $\omega_L = 977.3 \text{ cm}^{-1}$, $\epsilon_{\infty} = 6.49$, and $\gamma = 2 \text{ cm}^{-1}$ [43,44]. The new modes, illustrated by peaks in the colormap, split around the bare SPhP frequency and as the film thins are pushed closer to asymptotic ($d \rightarrow 0$) frequencies at ω_L and ω_T .

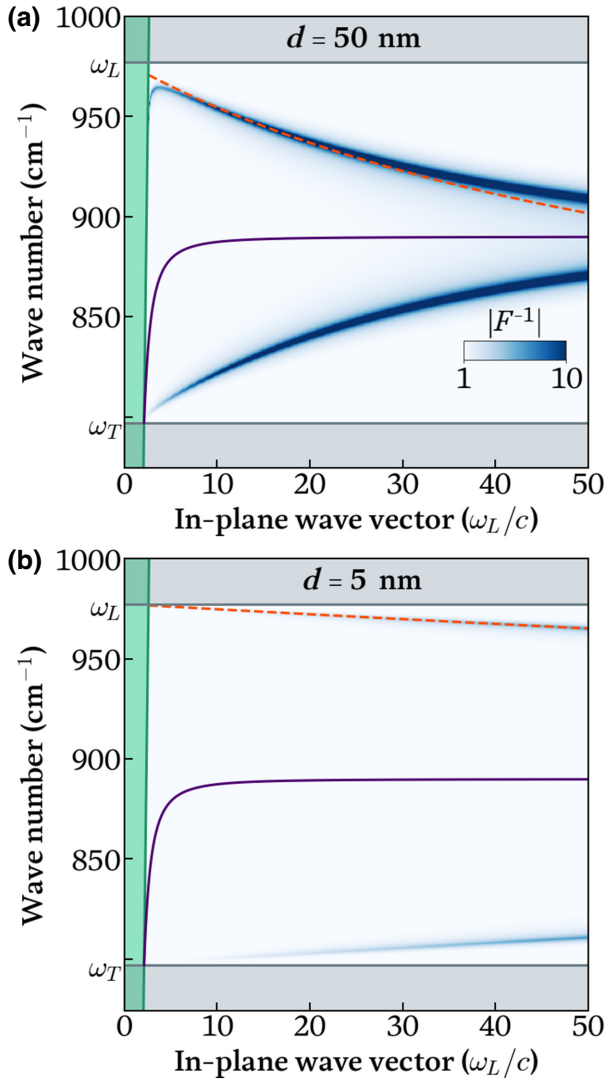


FIG. 2. Modal dispersion for a 50 nm (a) and 5 nm (b) 3C-SiC waveguide between high index ($n = 2.6$) cladding layers. The white region illustrates the spectral extent of the Reststrahlen between ω_T and ω_L , where SPhPs are supported. The leaky region within the light line is shaded in green. The analytical ENZ dispersion from Eq. (4) is shown by the dashed red line, and the bilayer SPhP dispersion by the solid purple curve.

In the limit $\alpha_2 d \ll 1$, focusing on the symmetric blue-shifted mode, we can rewrite Eq. (1) as

$$\frac{\epsilon_2}{\epsilon_1} + \frac{|\mathbf{k}|d}{2} = 0, \quad (3)$$

where we have taken the small argument limit $\tanh(\alpha_2 d) \approx \alpha_2 d$, assumed a large in-plane wave vector $\alpha_1 \approx |\mathbf{k}|$, and noted that close to ω_L we have $\epsilon_2(\omega) \approx 0$ and thus $\epsilon_2(\omega)k_0^2 \ll |\mathbf{k}|^2$, and $\epsilon_2(\omega)^2 \ll \epsilon_1^2$. In this regime the excitation is typically termed an ENZ mode [45]. These are of great interest as the vanishing dielectric function $\epsilon_2 \rightarrow 0$ leads to a very strong enhancement in the out-of-plane field

in the thin film with applications in low-loss waveguiding [21], vibrational spectroscopy [46], superscattering of light [47], manipulating of thermal emission [48], and altering light-matter interactions [49]. Solving for ω we can find the ENZ mode frequency as a function of in-plane wave vector \mathbf{k} :

$$\tilde{\omega}_{\text{ENZ},\mathbf{k}} = \sqrt{\frac{\omega_L^2 + |\mathbf{k}|q\omega_T^2}{1 + |\mathbf{k}|q} - (\gamma/2)^2} - \frac{i\gamma}{2}. \quad (4)$$

Here $q = d\epsilon_1/2\epsilon_\infty$ and we use a tilde to indicate a complex frequency. This result is valid for a finite range of in-plane wave vectors because, as discussed above, when $|\mathbf{k}|$ becomes large, the small argument approximation breaks down. The calculated ENZ dispersion $\omega_{\text{ENZ},\mathbf{k}}$ is shown by red dashed lines in Figs. 2(a) and 2(b), where it is clear that the approximations from Eq. (4) are less accurate for thicker films and larger in-plane wave vectors.

Nonlocal effects in polar dielectrics have been studied both theoretically [26,28,50] and experimentally [38] in layered nanostructures called hybrid crystals. Importantly, in a nonlocal model phonons do not exist solely at fixed frequencies, instead they are dispersive. Solving the ionic equation of motion (Eq. A1 of Ref. [26]) for longitudinally polarized modes leads to complex out-of-plane wave vectors

$$\xi = \sqrt{\frac{\omega(\omega + i\gamma) - \omega_L^2}{\beta_L^2} + |\mathbf{k}|^2}, \quad (5)$$

where ω_L is the bulk LO phonon frequency, ω is the driving frequency, and β_L is the LO phonon propagation velocity. In Ref. [26] we demonstrated that thin polar films of width d clad by phonon inactive layers act as Fabry-Pérot resonators for LO phonons, supporting discrete modes whose real ($\gamma \rightarrow 0$) resonant frequencies can be written

$$\omega_{n,\mathbf{k}} = \sqrt{\omega_L^2 - \beta_L^2(\xi_n^2 + |\mathbf{k}|^2)}, \quad (6)$$

where $\xi_n = (n+1)\pi/d$ is the discrete out-of-plane phonon wave vector [28]; this notation has been chosen for clarity so that the algebraic and geometric parity of the modes are the same. Note that, contrary to photonic Fabry-Pérot resonators, higher-order phonon modes are red shifted due to the negative dispersion of optical phonons at small wave vectors. We plot the spectrum $\omega_{n,\mathbf{k}}$ for 3C-SiC films in Fig. 3, using horizontal dashed lines for 10 nm (top panels) and 5 nm (bottom panels) film thicknesses. Here we use 3C-SiC phonon velocity $\beta_L = 15.39 \times 10^5 \text{ cm s}^{-1}$, derived from the bulk phonon dispersion [51]. Note that, within the interval of in-plane wave vectors considered $\beta_L|\mathbf{k}| \ll \omega_L - \omega_T$, the phonons do not appreciably disperse; for this reason, we approximate longitudinal mode frequencies by their zone-center values $\omega_n \approx \omega_{n,0}$. In the

same figures the local ENZ dispersion from Eq. (4) is shown by a red dashed line. In thinner films out-of-plane momentum ξ_n grows and phonon branches red shift away from ω_L .

We are interested in the nonlocal response of the ENZ excitation. We also consider longitudinal phonons in the central layer, with electric field given by

$$\mathbf{E}_L^\pm = \frac{e^{i\mathbf{k}\cdot\mathbf{r}}}{\sqrt{2}} \left[\begin{pmatrix} 1 \\ 0 \\ -i\xi/|\mathbf{k}| \end{pmatrix} e^{\xi z} \pm \begin{pmatrix} 1 \\ 0 \\ i\xi/|\mathbf{k}| \end{pmatrix} e^{-\xi(z+d)} \right], \quad (7)$$

where the “ \pm ” labels the parity of the phonon field and \mathbf{r} labels in-plane Cartesian coordinates.

We demonstrated in Ref. [26] that the full nonlocal dispersion can be found by applying the Maxwell boundary conditions on the in-plane field components $\mathbf{H}_\parallel, \mathbf{E}_\parallel$ and a single nonlocal additional boundary condition on the out-of-plane one $\epsilon_\infty E_\perp$. These conditions lead to a nonlocal dispersion relation $G = 0$ (derived in Appendix A), where

$$G = \tanh\left(\frac{\alpha_2 d}{2}\right) + \frac{\alpha_1 \epsilon_2}{\alpha_2 \epsilon_1} + \tanh\left(\frac{\xi d}{2}\right) \left(\frac{\epsilon_2}{\epsilon_\infty} - 1\right) \frac{|\mathbf{k}|^2}{\xi \alpha_2}. \quad (8)$$

Note that here only phonons of equal parity to the ENZ field [“ $-$ ” branch of Eq. (7)] participate in the coupling in a symmetric waveguide. We plot the inverse of the dispersion $|G^{-1}|$ as a colormap in Fig. 3. The left panels (a),(c) correspond to the local ($\beta_L = 0$) case, while the right panels (b),(d) show the nonlocal case. The top (a),(b) and bottom (c),(d) panels correspond to 10 and 5 nm SiC films, respectively. Compared to the local case we see that nonlocality leads to the appearance of anticrossings between the ENZ mode and even-numbered localized phonon branches, with increasing coupling for higher n phonons. These even-numbered branches correspond to solutions where the out-of-plane electric field vanishes at the film edge.

Having theoretically described the spectrum of the system, and shown the appearance of multiple strong-coupling features, we now want to derive from Eq. (8) a more transparent description of the nonlocality-mediated coupling. The key step to pass from a holistic description to a modal one is to expand the hyperbolic function on the right of Eq. (8) utilizing Mittag-Leffler’s theorem. This permits us to express a meromorphic function as a sum of partial fractions. Meromorphic functions are holomorphic at all points in the complex plane, except for a set of isolated poles. The standard expression for the series expansion of \tanh is given by

$$\tanh(z) = \sum_{n=0}^{\infty} \frac{8z}{(2n+1)\pi^2 + 4z^2}. \quad (9)$$

For $z = \xi d/2$, this equation informs us that the poles of the meromorphic function satisfy the relation $(2n+1)^2 \pi^2/d^2 + \xi^2 = 0$. Utilizing the nonlocal dispersion relation Eq. (8), we can write

$$\frac{(2n+1)^2 \pi^2}{d^2} + \xi^2 = \frac{(2n+1)^2 \pi^2}{d^2} + \frac{\omega(\omega + i\gamma) - \omega_L^2}{\beta_L} + |\mathbf{k}|^2, \quad (10)$$

which allows us to write the LO phonon component of Eq. (8) in the form

$$\begin{aligned} \frac{\tanh(\xi d/2)}{\xi} &= \frac{d}{2} \sum_{n=0}^{\infty} \frac{8}{(2n+1)^2 \pi^2 + \xi^2 d^2} \\ &= \frac{d}{2} \sum_{n \text{ even}} \frac{8\beta_L^2/d^2}{\omega(\omega + i\gamma) - \omega_n^2}, \end{aligned} \quad (11)$$

where the discrete phonon frequencies for even values of n are given by are given by Eq. (6). In so doing we have moved from a continuum representation of the LO field where the hyperbolic \tanh helps the full, combined response of the LO field, to one where each term on the right uniquely contains all information associated with the resonance labeled n . Now utilizing result (11) and the ENZ approximations discussed earlier, we can transform the transcendental Eq. (8) into the factorized dispersion relation

$$1 = \frac{\omega_L^2 - \omega_{\text{ENZ},\mathbf{k}}^2}{\omega_{\text{ENZ},\mathbf{k}}^2 - \omega(\omega + i\gamma)} \sum_{n \text{ even}} \frac{8\beta_L^2/d^2}{\omega_n^2 - \omega(\omega + i\gamma)}, \quad (12)$$

where $\omega_{\text{ENZ},\mathbf{k}}$ is the ENZ mode frequency from Eq. (4) in the limit $\gamma \rightarrow 0$. The polaritonic frequencies obtained from this equation are plotted as solid yellow lines in Figs. 3(b) and 3(e) for $\gamma \rightarrow 0$, demonstrating excellent agreement between the polaritonic model and the full dispersion map.

In order to develop a modal, quantum description of the hybrid longitudinal-transverse polaritons that can be used to both directly link the system spectrum to the geometric and material device parameters, and to provide a way to calculate the rates of polariton generation and scattering, we start by introducing second-quantized operators for the bare modes. We thus define $\hat{a}_{\mathbf{k}}^\dagger$ as the creation operator for an ENZ mode with in-plane wave vector \mathbf{k} and $\hat{b}_{n,\mathbf{k}}^\dagger$ for the n th discrete longitudinal phonon mode of the layer. The coupling between resonances can be described by a generic, phenomenological Hamiltonian modeling resonant energy exchange between the transverse ENZ and the

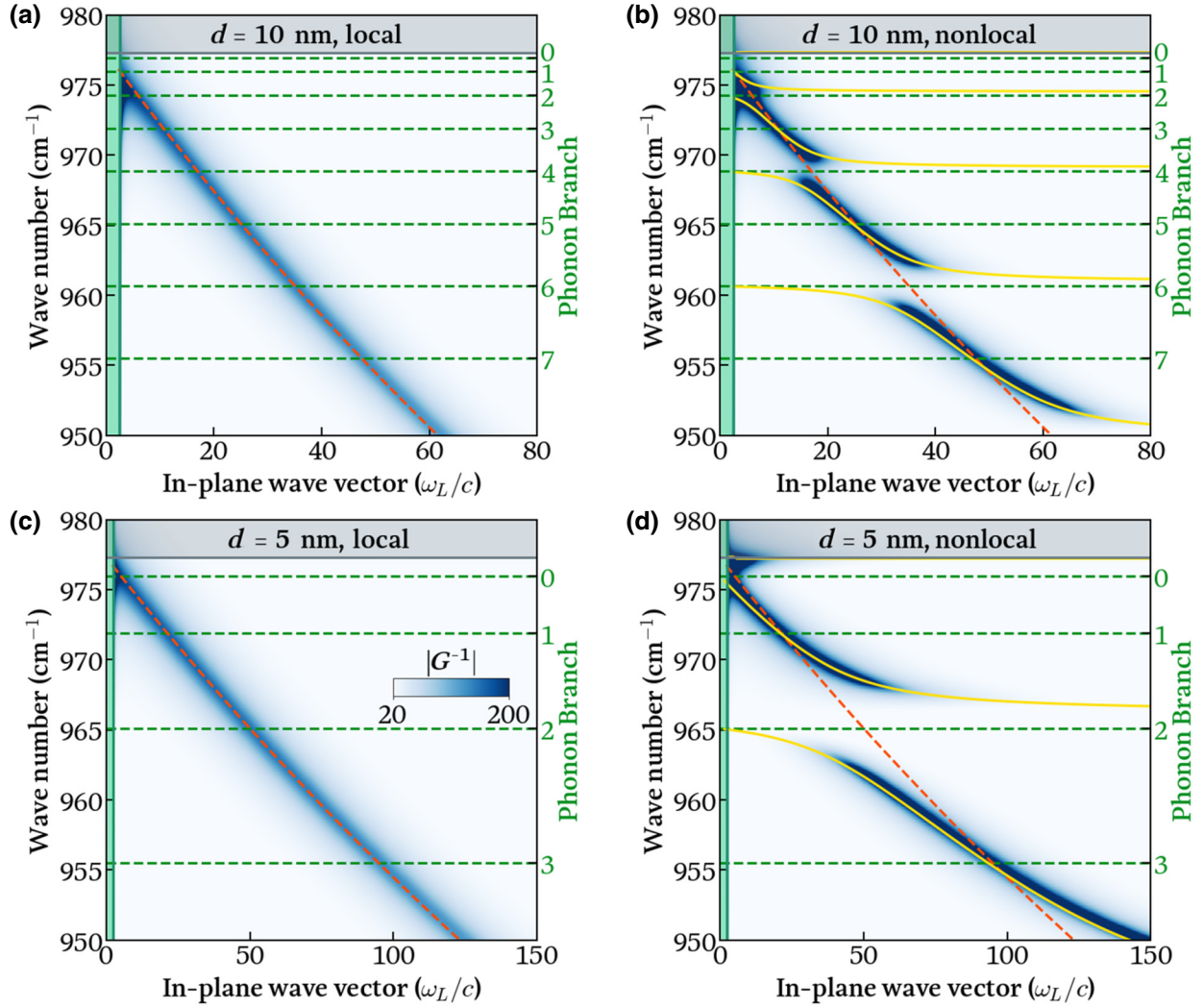


FIG. 3. Local (a) and nonlocal (b) dispersion relations for a 10 nm SiC film. Localized phonon frequencies $\omega_{n,\mathbf{k}}$ from Eq. (6) are illustrated with green dashed lines, with darker colors corresponding to higher-order modes. The red dashed line indicates the ENZ dispersion from Eq. (4). Solid yellow lines indicate calculated polariton frequencies. (c),(d) The lower panels show the same for a 5 nm SiC film. The color scale is uniform across all panels.

longitudinal phonons

$$\hat{\mathcal{H}} = \sum_{\mathbf{k}} \left\{ \hbar\omega_{\text{ENZ},\mathbf{k}} \hat{a}_{\mathbf{k}}^\dagger \hat{a}_{\mathbf{k}} + \sum_{n \in \text{even}} \left[\hbar\omega_n \hat{b}_{n,\mathbf{k}}^\dagger \hat{b}_{n,\mathbf{k}} + \frac{\hbar\Theta_{n,\mathbf{k}}}{2} (\hat{a}_{-\mathbf{k}}^\dagger + \hat{a}_{\mathbf{k}}) (\hat{b}_{n,\mathbf{k}}^\dagger + \hat{b}_{n,-\mathbf{k}}) \right] \right\}, \quad (13)$$

where $\Theta_{n,\mathbf{k}}$ is the n th phonon coupling frequency at common in-plane wave vector \mathbf{k} . The eigenvalue equation for this Hamiltonian can be written considering polariton operators of the form

$$\hat{d}_{\mathbf{k}} = \alpha_{\mathbf{k}} \hat{a}_{\mathbf{k}} + \zeta_{\mathbf{k}} \hat{a}_{-\mathbf{k}}^\dagger + \sum_{n \in \text{even}} \beta_{n,\mathbf{k}} \hat{b}_{n,\mathbf{k}} + \theta_{n,\mathbf{k}} \hat{b}_{n,-\mathbf{k}}^\dagger, \quad (14)$$

where Greek letters are Hopfield coefficients [32]. In order for $\hat{d}_{\mathbf{k}}$ to diagonalize the Hamiltonian $\hat{\mathcal{H}}$, it must satisfy the eigenequation

$$[\hat{d}_{\mathbf{k}}, \hat{\mathcal{H}}] = \hbar\omega \hat{d}_{\mathbf{k}}, \quad (15)$$

where ω is the frequency of the coupled mode. As shown in Appendix B, by expanding the commutator in Eq. (15), collecting terms proportional to each operator in Eq. (13) on each side, and eliminating the Hopfield coefficients we recover the secular dispersion relation

$$1 = \frac{\omega_{\text{ENZ},\mathbf{k}}}{\omega_{\text{ENZ},\mathbf{k}}^2 - \omega^2} \sum_{n \in \text{even}} \frac{|\Theta_{n,\mathbf{k}}|^2 \omega_n}{\omega_n^2 - \omega^2}, \quad (16)$$

whose roots provide the polariton eigenfrequencies of the system. Note that, although we have ignored losses in the quantum model, leading to a disparity between Eqs. (16) and (4), they could be included by coupling Eq. (13) to a thermal bath [20]. By comparison with Eq. (12) we can then directly derive one of the key results of this work, that is, the analytical expression of the longitudinal-transverse coupling

$$|\Theta_{n,\mathbf{k}}|^2 = \frac{\omega_L^2 - \omega_{\text{ENZ},\mathbf{k}}^2}{\omega_{\text{ENZ},\mathbf{k}}\omega_n} \frac{8\beta_L^2}{d^2}. \quad (17)$$

We can already see that the coupling increases linearly with β_L/d , quantifying our physical intuition that the nonlocality-mediated coupling increases when phonon propagation cannot be neglected (large β_L) and for smaller structures (small d).

To illustrate the physical content of Eq. (12), we specialize onto the case where only the n th phonon branch is near resonant with the ENZ mode and the others can be safely neglected, yielding polariton frequencies

$$\omega_{\pm,\mathbf{k}}^2 = \frac{\omega_{\text{ENZ},\mathbf{k}}^2 + \omega_n^2}{2} \pm \frac{\sqrt{(\omega_{\text{ENZ},\mathbf{k}}^2 - \omega_n^2)^2 + 4|\Theta_{n,\mathbf{k}}|^2\omega_{\text{ENZ},\mathbf{k}}\omega_n}}{2}. \quad (18)$$

The vacuum Rabi frequency, defined as half the resonant polariton splitting at the anticrossing $\omega_{\text{ENZ},\mathbf{k}} = \omega_n$, can thus be written as

$$\Omega_R = \frac{\omega_{+,\mathbf{k}} - \omega_{-,\mathbf{k}}}{2}. \quad (19)$$

This quantity determines the coupling regime of the system. When Ω_R is smaller than the linewidths, the system is in weak coupling, while when it is appreciably larger, we can resolve the polaritonic splitting and the system is in the strong coupling regime. In the small coupling regime we can write the Rabi frequency, normalized by the anticrossing frequency, as

$$\frac{\Omega_R}{\omega_n} = \frac{\sqrt{2}}{\xi_n d (\omega_L^2 / \Delta\omega_n^2 - 1)}, \quad (20)$$

where the longitudinal mode frequency shift $\Delta\omega_n = \beta_L^2 \xi_n^2$ describes the departure in the n th phonon frequency from its zone-center frequency. The result demonstrates two routes to increasing the Rabi frequency through tuning the phonon component: either through considering higher-order (larger n) modes or exploiting materials with larger phonon velocity β_L to increase $\Delta\omega_n$.

The d^{-1} remaining in Eq. (20) arises from the ENZ mode's out-of-plane electric field in the central layer as $|E_{z,\mathbf{k}}| \propto d^{-1}$ following Campione [45].

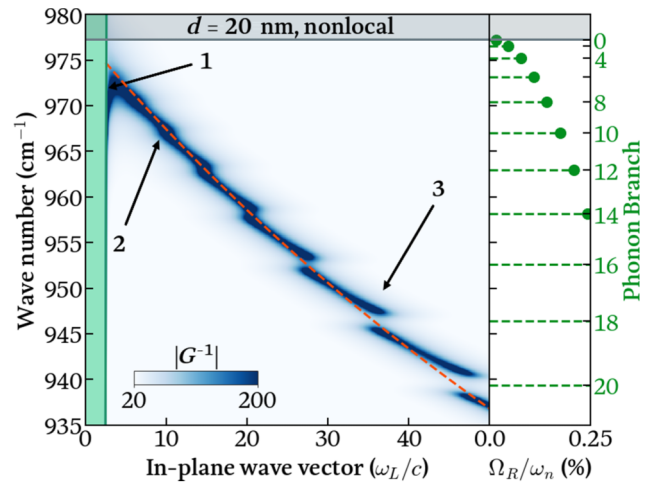


FIG. 4. Full dispersion relations from Eq. (8) for a film thickness of 20 nm; right panel shows the predicted normalized Rabi frequencies Ω_R/ω_n . Labeled arrows refer to regions of the plot discussed in the text.

This implies that, for a general structure, the coupling strength can be enhanced by increasing the photonic field strength at the nonlocal interface. This could allow for larger photon-phonon coupling rates in nanophotonic structures where the photon field is confined in multiple dimensions through Purcell factor optimization [20,40].

To explore the transition between the weak and strong coupling regimes, with the opening of the polaritonic gap, we consider a wider structure, in order to have access to more phonon modes in the Reststrahlen region. In Fig. 4 we thus plot the dispersion of a 20 nm 3C-SiC film, with three qualitatively different regions highlighted. In region 1 the ENZ mode instead initially follows the light line in the cladding, before coalescing with the analytical dispersion, Eq. (4), at larger wave vector. This small wave vector region is not well captured by our Hamiltonian model because near to the light line the approximation $\alpha_2 \approx |\mathbf{k}|$ utilized to derive Eq. (3) fails. In this small wave vector regime there is no simple analytical dispersion relation for the ENZ excitation [45]. In region 2 larger n causes an increase in ENZ linewidth where the ENZ dispersion crosses the localized phonon one. In this region localized phonons act as loss channels, extracting energy from the ENZ mode, but as Ω_R is smaller than the linewidth, the energy is lost before it can cycle back. In region 3 the polariton frequencies are sufficiently far from ω_L , strong coupling is established, and anticrossings emerge in the spectra. The evolution of the normalized coupling Ω_R/ω_n is shown in panel (b), highlighting the expected increase for higher-order modes.

There is a final parameter that determines whether the system is in weak or strong coupling that does not enter the coupling frequency (17), which is the modal damping rate. When this exceeds the Rabi frequency, the

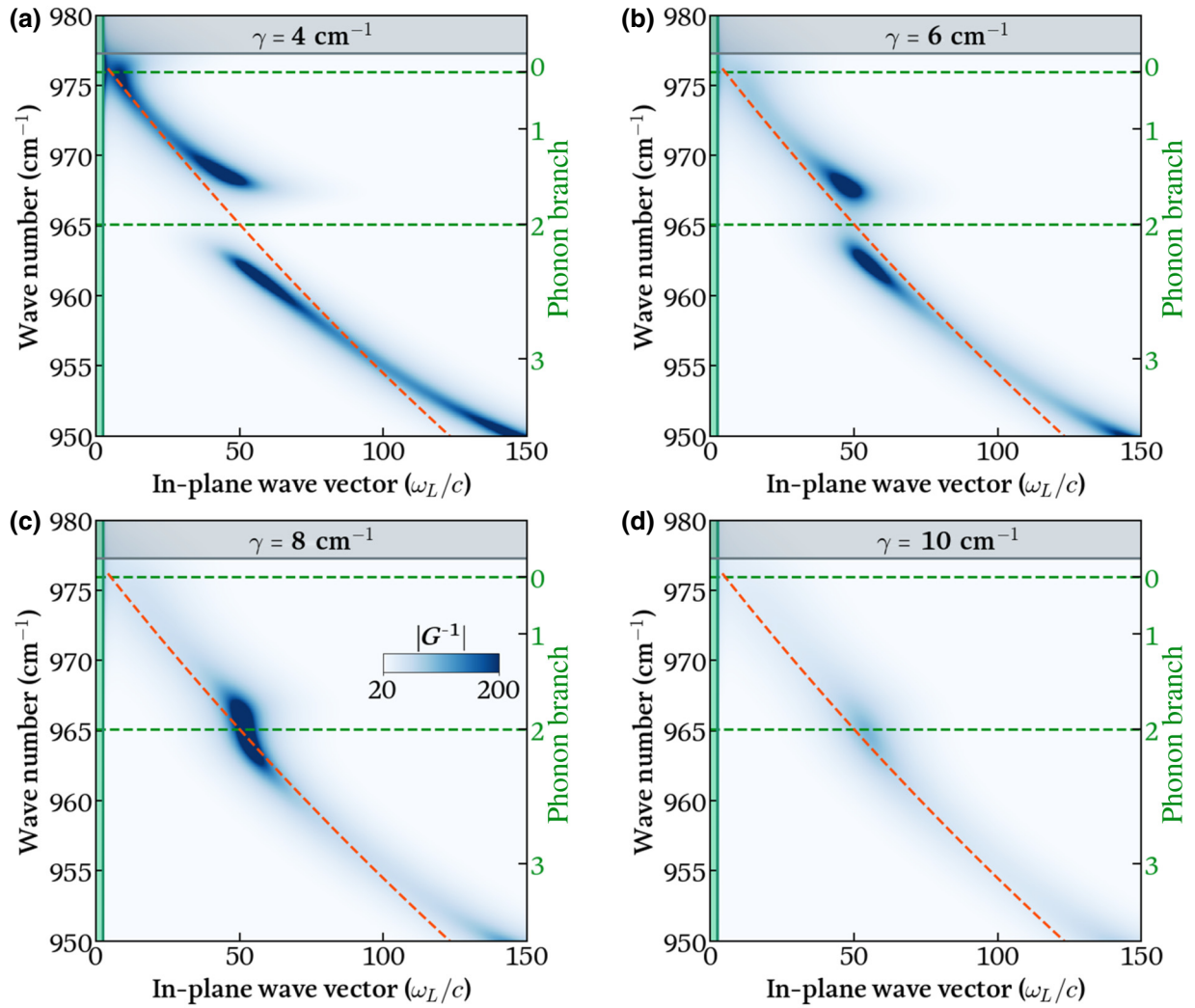


FIG. 5. Nonlocal dispersion relations for a 5 nm 3C-SiC layer, analogous to Fig. 3(d), for various values of the loss parameter γ . Panels show (a) $\gamma = 4 \text{ cm}^{-1}$, (b) $\gamma = 6 \text{ cm}^{-1}$, (c) $\gamma = 8 \text{ cm}^{-1}$, (d) $\gamma = 10 \text{ cm}^{-1}$. The red dashed line indicates the ENZ dispersion from Eq. (4). Increasing the losses, reduces the anticrossing until it eventually disappears, as the system passes from the strong to the weak coupling regime.

system's modes are in weak coupling, while in the opposite regime they are in strong coupling and coherently exchange energy. Now we increase the losses while keeping geometry and other material parameters determining the coupling strength fixed, allowing us to pass through the weak to strong coupling transition. This is important not only in view of applications of our theory to other materials, but even for the case of 3C-SiC, which we chose for its preponderance as a testbed for phonon-polariton physics [3,4,40,52,53]. We have in fact used the 3C-SiC bulk value for $\gamma = 2 \text{ cm}^{-1}$ [43], but high-quality nanoscale 3C-SiC films are typically grown on silicon, and ultrathin films can be expected to have high defect densities, increasing material loss. We have moreover neglected that LO phonons are reported to have marginally larger losses than transverse ones [44].

To illustrate the effect of material loss on the nonlocal physics, we study the 5 nm structure investigated earlier with increased damping rates. The results are shown in Fig. 5 for damping rates of $\gamma = 4, 6, 8, 10 \text{ cm}^{-1}$. Note that, for this structure, the vacuum Rabi frequency with the $n = 2$ LO phonon branch is estimated through Eq. (20) as $\Omega_R = 3.7 \text{ cm}^{-1}$. In panel (a), where $\gamma \approx \Omega_R$, the system response is very similar to that in Fig. 3(d), where $\gamma = 2 \text{ cm}^{-1}$. The system remains in strong coupling. When γ is increased to 6 cm^{-1} in panel (b), the anticrossing is reduced but still visible. In panels (c) and (d), where γ is increased to 8 and 10 cm^{-1} , respectively, the anticrossing vanishes and the system passes into the weak coupling regime. This is a combination of two physical effects: firstly, the damping rate has increased with respect to the Rabi frequency and, secondly, the nonlocal figure of merit, which

is the skin depth of the LO phonon $L = \text{Im}\{\xi\}^{-1}$ [26], has decreased sufficiently such that the thin film no longer possesses a discrete phonon spectrum. When $\gamma = 4 \text{ cm}^{-1}$, we find that $L = 1.3d$, while when $\gamma = 10 \text{ cm}^{-1}$, we recover $L = 0.53d$. At higher damping rates LO phonons can no longer transport energy between the two interfaces of the central film, instead they just act as an additional loss channel for the ENZ mode.

These effects can be mitigated utilizing methods such as vapor-liquid-solid growth, which allow for the fabrication of high-quality subnanometer SiC films [54]. Additionally, alternative materials, particularly those which can be grown in high-quality thin films by atomic layer deposition on lattice-matched substrates such as AlN or GaN, can be utilized. Nonlocality in these anisotropic systems is expected to be physically similar to that presented in this work [28]. A second mitigation tactic is obvious through Eq. (20): by decreasing the film thickness, the coupling frequency is enhanced. This is a particularly promising route to explore nonlocal effects in systems grown by atomic layer deposition where high-quality films can be grown down to the true nanometer scale. For the parameters used in this work ($\beta_L = 15.39 \times 10^5 \text{ cms}^{-1}$, $\gamma = 2 \text{ cm}^{-1}$), this yields an onset at $d \approx 4 \text{ nm}$ for the $n = 2$ phonons. A final method to reach strong coupling could be utilizing isotopically pure polar dielectrics, which have been shown to support SPhPs with narrower linewidths than in naturally occurring materials [55].

We have demonstrated that the full nonlocal Maxwell equations supplemented by the proper mechanical boundary conditions lead naturally to a multimodal theory of ENZ modes coupled to localized phonon modes in the nonlocal dielectric nanolayer. Our theory provides a polaritonic description of the nanolayer physics that allows us to naturally integrate polariton scattering and generation in a fully quantum picture. To this end, we exploit the Mittag-Leffler expansion as a link between the polynomial dispersion relations yielded by a coupled mode theory and those found using the full nonlocal Maxwell's equations, allowing us to condense the complexity of the nonlocality-mediated coupling in a single coupling frequency dependent on geometric and material parameters. As an example of the design power provided by our results, we could thus directly calculate the minimal layer thickness for a fixed material, leading to the appearance of strong coupling and LTP modes. Although the nonlocal effects studied in this paper occur far outside the light line, they could be observed in a simple experiment by incorporating a metallic grating into the waveguide structure to fold the modes toward the zone center [3,20]. The nonlocal trilayer model with localized phonons we considered provides a quantitative tool to study a large fraction of the technologically relevant nonlocal nanophotonic samples fabricated by atomic layer deposition, as long as the Reststrahlen bands of interfacing materials do not significantly overlap.

In these systems LO mode frequencies are determined by the thicknesses of the nanoscale layers and are independent of the transverse dimensions that greatly exceed the phonon propagation length. Furthermore, our technique, derived in a specific system, could be expanded to more general settings, providing a powerful modal picture to study nonlocal optical nanodevices. One topic in which our theory could prove particularly effective is in the modeling of theoretically predicted devices powered by direct energy transfer between electrical currents and SPhPs mediated by the longitudinal-transverse hybridization. In these devices longitudinal-transverse polaritons act as interconnects between electronic and photonic systems, allowing for electronic generation or detection of light without the need for the quantum engineered electronic bandgaps typically utilized in midinfrared devices [56]. Utilizing longitudinal-transverse polaritons, it is possible to simplify and shrink optoelectronic devices, potentially allowing for the development of nanoscale midinfrared nanoemitters [57].

ACKNOWLEDGMENTS

The authors would like to thank Thomas G. Folland for fruitful discussions. S.D.L. is supported by a Royal Society Research fellowship and the Philip Leverhulme prize. The authors acknowledge support from the Royal Society Grant No. RGF\EA\181001 and the Leverhulme Grant No. RPG-2019-174.

APPENDIX A: MACROSCOPIC DISPERSION RELATIONS

The electric fields of the SPhPs at the upper and lower boundaries of the central film considered in this paper can be written as [42]

$$\mathbf{E}_{u,\mathbf{k}} = \begin{cases} \begin{bmatrix} \alpha_1 \epsilon_2 \left[\frac{\mathbf{k}}{|\mathbf{k}|}, -\frac{i|\mathbf{k}|}{\alpha_1} \right]^T \\ \alpha_2 \epsilon_C \left[\frac{\mathbf{k}}{|\mathbf{k}|}, \frac{i|\mathbf{k}|}{\alpha_2} \right]^T \end{bmatrix} e^{\alpha_1(z+d)} e^{i\mathbf{k}\cdot\mathbf{r}}, & z < -d, \\ -\begin{bmatrix} \frac{\mathbf{k}}{|\mathbf{k}|}, \frac{i|\mathbf{k}|}{\alpha_2} \end{bmatrix}^T e^{-\alpha_2(z+d)} e^{i\mathbf{k}\cdot\mathbf{r}}, & -d < z < 0, \\ -\begin{bmatrix} \alpha_1 \epsilon_2 \left[\frac{\mathbf{k}}{|\mathbf{k}|}, \frac{i|\mathbf{k}|}{\alpha_1} \right]^T \\ \alpha_2 \epsilon_1 \left[\frac{\mathbf{k}}{|\mathbf{k}|}, \frac{i|\mathbf{k}|}{\alpha_1} \right]^T \end{bmatrix} e^{-\alpha_1 z - \alpha_2 d} e^{i\mathbf{k}\cdot\mathbf{r}}, & z > 0, \end{cases} \quad (\text{A1})$$

$$\mathbf{E}_{l,\mathbf{k}} = \begin{cases} \begin{bmatrix} \alpha_1 \epsilon_2 \left[\frac{\mathbf{k}}{|\mathbf{k}|}, -\frac{i|\mathbf{k}|}{\alpha_1} \right]^T \\ \alpha_2 \epsilon_1 \left[\frac{\mathbf{k}}{|\mathbf{k}|}, \frac{i|\mathbf{k}|}{\alpha_2} \right]^T \end{bmatrix} e^{\alpha_1(z+d) - \alpha_2 d} e^{i\mathbf{k}\cdot\mathbf{r}}, & z < -d, \\ \begin{bmatrix} \frac{\mathbf{k}}{|\mathbf{k}|}, -\frac{i|\mathbf{k}|}{\alpha_2} \end{bmatrix}^T e^{\alpha_2 z} e^{i\mathbf{k}\cdot\mathbf{r}}, & -d < z < 0, \\ -\begin{bmatrix} \alpha_1 \epsilon_2 \left[\frac{\mathbf{k}}{|\mathbf{k}|}, \frac{i|\mathbf{k}|}{\alpha_1} \right]^T \\ \alpha_2 \epsilon_1 \left[\frac{\mathbf{k}}{|\mathbf{k}|}, \frac{i|\mathbf{k}|}{\alpha_1} \right]^T \end{bmatrix} e^{-\alpha_1 z} e^{i\mathbf{k}\cdot\mathbf{r}}, & z > 0, \end{cases} \quad (\text{A2})$$

where we have defined the in-plane wave vector \mathbf{k} so that the full three-dimensional (3D) wave vector is $[\mathbf{k}, \alpha_i]$ and similarly for the 3D coordinate $[\mathbf{r}, z]$, and the out-of-plane wave vectors α_i have been rotated into the complex plane. The magnetic field can be found utilizing the Maxwell-Faraday equation as

$$\mathbf{H}_{u,\mathbf{k}} = \frac{i\omega\epsilon_2}{c^2\alpha_2} \left[\hat{\mathbf{z}} \times \frac{\mathbf{k}}{|\mathbf{k}|}, 0 \right]^T e^{i\mathbf{k}\cdot\mathbf{r}} \begin{cases} e^{\alpha_1(z+d)}, & z < -d, \\ e^{-\alpha_2(z+d)}, & -d < z < 0, \\ e^{-\alpha_1 z - \alpha_2 d}, & z > 0, \end{cases} \quad (\text{A3})$$

$$\mathbf{H}_{l,\mathbf{k}} = \frac{i\omega\epsilon_2}{c^2\alpha_2} \left[\hat{\mathbf{z}} \times \frac{\mathbf{k}}{|\mathbf{k}|}, 0 \right]^T \times e^{i\mathbf{k}\cdot\mathbf{r}} \begin{cases} e^{\alpha_1(z+d) - \alpha_2 d}, & z < -d, \\ e^{\alpha_2 z}, & -d < z < 0, \\ e^{-\alpha_1 z}, & z > 0, \end{cases} \quad (\text{A4})$$

where we have constructed the fields to fulfill the boundary condition on the tangential magnetic field. The total field in the waveguide is a linear superposition of the SPhPs at the upper and lower interfaces

$$\mathbf{E} = U\mathbf{E}_{u,\mathbf{k}} + L\mathbf{E}_{l,\mathbf{k}}, \quad (\text{A5})$$

which, applying the Maxwell boundary condition on the tangential electric field at the upper and lower edges of the film $z = 0, z = -d$, leads to the matrix equation

$$\begin{pmatrix} [\alpha_1\epsilon_2/(\alpha_2\epsilon_1) - 1]e^{-\alpha_2 d} & 1 + \alpha_1\epsilon_2/(\alpha_2\epsilon_1) \\ \alpha_1\epsilon_2/(\alpha_2\epsilon_1) + 1 & [\alpha_1\epsilon_2/(\alpha_2\epsilon_1) - 1]e^{-\alpha_2 d} \end{pmatrix} \times \begin{pmatrix} U \\ L \end{pmatrix} = \begin{pmatrix} 0 \\ 0 \end{pmatrix}. \quad (\text{A6})$$

This equation is satisfied when the determinant is nil, or

$$1 - r_{21}^2 e^{-2\alpha_2 d} = 0, \quad (\text{A7})$$

where r_{21} is the Fresnel reflection coefficient

$$r_{21} = \frac{\alpha_2\epsilon_1 - \alpha_1\epsilon_2}{\alpha_2\epsilon_1 + \alpha_1\epsilon_2}. \quad (\text{A8})$$

Utilizing the standard hyperbolic identities, we can rewrite this dispersion relation as

$$0 = 2 \left[1 - \tanh(\alpha_2 d) \frac{r_{21}^2 + 1}{r_{21}^2 - 1} \right], \quad (\text{A9})$$

which in turn reduces to Eq. (1) in the main text.

To derive the dispersion relation of the epsilon-near-zero mode, we consider the case $L = U$ that corresponds

to the symmetric excitation in the waveguide. In this case the rows of Eq. (A6) are degenerate, yielding

$$\frac{\alpha_1\epsilon_2}{\alpha_2\epsilon_1} + \tanh\left(\frac{\alpha_2 d}{2}\right) \approx \frac{\alpha_1\epsilon_2}{\alpha_2\epsilon_1} + \frac{\alpha_2 d}{2} = 0, \quad (\text{A10})$$

where we have utilized the small argument approximation of the hyperbolic tanh, valid for $\alpha_2 d \ll 1$. Note that this reduces to Eq. (3) in the limit $|\mathbf{k}|/k_0 \gg 1$.

We can derive the nonlocal dispersion relation from the electric fields of the SPhPs given in Eqs. (A1) and (A2) and the field of the longitudinal phonon, Eq. (7) given in the main text. Focusing on the symmetric excitation $L = U$ we can write the boundary matrix formed from continuity of the transverse electric field and the out-of-plane projection $\epsilon_\infty \hat{\mathbf{z}} \cdot \mathbf{E}$ doing so, we arrive at the matrix equation

$$\mathcal{M} \begin{pmatrix} X \\ Y \end{pmatrix} = \begin{pmatrix} 0 \\ 0 \end{pmatrix}, \quad (\text{A11})$$

where the coefficients X, Y weight the SPhP and LO phonon contributions, respectively. The matrix \mathcal{M} can be written after some manipulation in the form

$$\begin{pmatrix} 1 - r_{21}e^{-\alpha_2 d} & -\alpha_2\epsilon_1(1 - e^{-\xi d})/(\alpha_2\epsilon_1 + \alpha_1\epsilon_2) \\ [\epsilon_2/\epsilon_\infty - 1][1 + e^{-\alpha_2 d}] & \xi\alpha_2(1 + e^{-\xi d})/|\mathbf{k}|^2 \end{pmatrix}. \quad (\text{A12})$$

Finally, the dispersion of the coupled modes is given by $\det\{\mathcal{M}\} = 0$; expanding this relation leads to Eq. (8) in the main text.

APPENDIX B: HAMILTONIAN-DERIVED DISPERSION RELATIONS

In the main text we introduced the Hamiltonian of the coupled epsilon-near-zero and LO phonon ladder, Eq. (13), which is then diagonalized by introduction of the polaritonic operator (14) utilizing the Heisenberg equation of motion (15). In this appendix we detail this procedure, deriving from the Hamiltonian the secular Eq. (16) in the main text. To diagonalize the Hamiltonian, we first need to note the nonzero commutation relations between canonical operators entering Hamiltonian (13), which are

$$[\hat{a}_{\mathbf{k}}, \hat{a}_{\mathbf{q}}^\dagger] = \delta_{\mathbf{k}\mathbf{q}}, \quad (\text{B1a})$$

$$[\hat{b}_{m,\mathbf{k}}, \hat{b}_{n,\mathbf{q}}^\dagger] = \delta_{\mathbf{k}\mathbf{q}} \delta_{mn}. \quad (\text{B1b})$$

All other commutation operations, for example those between operators for epsilon-near-zero and LO phonon modes, are zero. Using this result, we can calculate the commutation relation entering Eq. (15). As the calculation is large, it is practical to proceed through the Hamiltonian

term by term. The commutator with the term describing the bare epsilon-near-zero mode is given by

$$\begin{aligned} & \left[\hat{d}_{\mathbf{k}}, \sum_{\mathbf{q}} \hbar \omega_{\text{ENZ},\mathbf{q}} \hat{a}_{\mathbf{q}}^{\dagger} \hat{a}_{\mathbf{q}} \right] \\ &= \sum_{\mathbf{q}} \hbar \omega_{\text{ENZ},\mathbf{q}} \{ \alpha_{\mathbf{k}} \hat{a}_{\mathbf{q}} \delta_{\mathbf{k}\mathbf{q}} - \zeta_{\mathbf{k}} \hat{a}_{\mathbf{q}}^{\dagger} \delta_{-\mathbf{k}\mathbf{q}} \} \\ &= \hbar \omega_{\text{ENZ},\mathbf{k}} \{ \alpha_{\mathbf{k}} \hat{a}_{\mathbf{k}} - \zeta_{\mathbf{k}} \hat{a}_{-\mathbf{k}}^{\dagger} \}, \end{aligned} \quad (\text{B2})$$

where we have utilized the system's translational invariance to note that $\omega_{\text{ENZ},\mathbf{k}} = \omega_{\text{ENZ},-\mathbf{k}}$. Similarly, for the bare phonon component, we can write

$$\begin{aligned} & \left[\hat{d}_{\mathbf{k}}, \sum_{\mathbf{q}} \sum_{m \in \text{even}} \hbar \omega_n \hat{b}_{m,\mathbf{q}}^{\dagger} \hat{b}_{m,\mathbf{q}} \right] \\ &= \sum_{n \in \text{even}} \hbar \omega_n \{ \beta_{n,\mathbf{k}} \hat{b}_{n,\mathbf{k}} - \theta_{n,\mathbf{k}} \hat{b}_{n,-\mathbf{k}}^{\dagger} \}. \end{aligned} \quad (\text{B3})$$

Finally, we can find the contribution from the interaction component of the Hamiltonian

$$\hat{\mathcal{H}}_{\text{int}} = \sum_{\mathbf{k}} \sum_{n \in \text{even}} \frac{\hbar \Theta_{n,\mathbf{k}}}{2} (\hat{a}_{-\mathbf{k}}^{\dagger} + \hat{a}_{\mathbf{k}}) (\hat{b}_{n,\mathbf{k}}^{\dagger} + \hat{b}_{n,-\mathbf{k}}), \quad (\text{B4})$$

which is given by

$$\begin{aligned} [\hat{d}_{\mathbf{k}}, \hat{\mathcal{H}}_{\text{int}}] &= \sum_{n \in \text{even}} \frac{\hbar \Theta_{n,\mathbf{k}}}{2} \{ (\alpha_{\mathbf{k}} - \zeta_{\mathbf{k}}) (\hat{b}_{n,-\mathbf{k}}^{\dagger} + \hat{b}_{n,\mathbf{k}}) \\ &\quad + (\beta_{n,\mathbf{k}} - \theta_{n,\mathbf{k}}) (\hat{a}_{-\mathbf{k}}^{\dagger} + \hat{a}_{\mathbf{k}}) \}. \end{aligned} \quad (\text{B5})$$

Now that we have computed the left-hand side of Eq. (15), we need to compare it to the right-hand side. As the equation is over operators, we collect like terms on each side to arrive at the polariton dispersion relation. The four equations of motion are given by

$$\hbar \omega \alpha_{\mathbf{k}} = \hbar \omega_{\text{ENZ},\mathbf{k}} \alpha_{\mathbf{k}} + \sum_{n \in \text{even}} \frac{\hbar \Theta_{n,\mathbf{k}}}{2} (\beta_{n,\mathbf{k}} - \theta_{n,\mathbf{k}}), \quad (\text{B6a})$$

$$\hbar \omega \zeta_{\mathbf{k}} = -\hbar \omega_{\text{ENZ},\mathbf{k}} \zeta_{\mathbf{k}} + \sum_{n \in \text{even}} \frac{\hbar \Theta_{n,\mathbf{k}}}{2} (\beta_{n,\mathbf{k}} - \theta_{n,\mathbf{k}}), \quad (\text{B6b})$$

$$\hbar \omega \beta_{n,\mathbf{k}} = \hbar \omega_n \beta_{n,\mathbf{k}} + \frac{\hbar \Theta_{n,\mathbf{k}}}{2} (\alpha_{\mathbf{k}} - \zeta_{\mathbf{k}}), \quad (\text{B6c})$$

$$\hbar \omega \theta_{n,\mathbf{k}} = -\hbar \omega_n \theta_{n,\mathbf{k}} + \frac{\hbar \Theta_{n,\mathbf{k}}}{2} (\alpha_{\mathbf{k}} - \zeta_{\mathbf{k}}), \quad (\text{B6d})$$

where, going in order, we have collected terms proportional to $\hat{a}_{\mathbf{k}}$, $\hat{a}_{-\mathbf{k}}^{\dagger}$, $\hat{b}_{n,\mathbf{k}}$, and $\hat{b}_{n,-\mathbf{k}}^{\dagger}$. We can solve these

equations by elimination of the Hopfield coefficients $\alpha_{\mathbf{k}}$, $\zeta_{\mathbf{k}}$, $\beta_{n,\mathbf{k}}$, $\theta_{n,\mathbf{k}}$. Taking the difference between the top and bottom pairs, we find that

$$\zeta_{\mathbf{k}} = \frac{\omega - \omega_{\text{ENZ},\mathbf{k}}}{\omega + \omega_{\text{ENZ},\mathbf{k}}} \alpha_{\mathbf{k}}, \quad (\text{B7a})$$

$$\theta_{n,\mathbf{k}} = \frac{\omega - \omega_n}{\omega + \omega_n} \beta_{n,\mathbf{k}}, \quad (\text{B7b})$$

which allows us to write the coefficient $\beta_{n,\mathbf{k}}$ in terms of $\alpha_{\mathbf{k}}$:

$$\beta_{n,\mathbf{k}} = \frac{\Theta_{n,\mathbf{k}}}{\omega - \omega_n} \frac{\omega_{\text{ENZ},\mathbf{k}}}{\omega + \omega_{\text{ENZ},\mathbf{k}}} \alpha_{\mathbf{k}}. \quad (\text{B8})$$

Hence, the first equation of motion becomes

$$\begin{aligned} (\omega - \omega_{\text{ENZ},\mathbf{k}}) \alpha_{\mathbf{k}} &= \sum_{n \in \text{even}} \frac{\Theta_{n,\mathbf{k}}}{2} \frac{2\omega_n}{\omega + \omega_n} \beta_{n,\mathbf{k}}, \\ &= \frac{\omega_{\text{ENZ},\mathbf{k}}}{\omega + \omega_{\text{ENZ},\mathbf{k}}} \sum_{n \in \text{even}} \frac{\Theta_{n,\mathbf{k}}^2 \omega_n}{\omega^2 - \omega_n^2} \alpha_{\mathbf{k}}, \end{aligned} \quad (\text{B9})$$

which on dividing through reduces to

$$1 = \frac{\omega_{\text{ENZ},\mathbf{k}}}{\omega_{\text{ENZ},\mathbf{k}}^2 - \omega^2} \sum_{n \in \text{even}} \frac{\Theta_{n,\mathbf{k}}^2 \omega_n}{\omega_n^2 - \omega^2}, \quad (\text{B10})$$

which is Eq. (16) in the main text.

-
- [1] D. Ballarini and S. De Liberato, Polaritonics: From microcavities to sub-wavelength confinement, *Nanophotonics* **8**, 641 (2019).
 - [2] J. Khurgin, Relative merits of phononics vs. plasmonics: The energy balance approach, *Nanophotonics* **7**, 2305 (2017).
 - [3] J.-J. Greffet, R. Carminati, K. Joulain, J.-P. Mulet, S. Mainy, and Y. Chen, Coherent emission of light by thermal sources, *Nature* **416**, 61 (2002).
 - [4] R. Hillenbrand, T. Taubner, and F. Keilmann, Phonon-enhanced light-matter interaction at the nanometre scale, *Nature* **418**, 159 (2002).
 - [5] J. D. Caldwell, L. Lindsay, V. Giannini, I. Vurgaftman, T. L. Reinecke, S. A. Maier, and O. J. Glembocki, Low-loss, infrared and terahertz nanophotonics using surface phonon polaritons, *Nanophotonics* **4**, 44 (2015).
 - [6] H. Sumikura, T. Wang, P. Li, A.-K. U. Michel, A. Heßler, L. Jung, M. Lewin, M. Wuttig, D. N. Chigrin, and T. Taubner, Highly confined and switchable mid-infrared surface phonon polariton resonances of planar circular cavities with a phase change material, *Nano Lett.* **19**, 2549 (2019).
 - [7] B. T. Spann, R. Compton, D. Ratchford, J. P. Long, A. D. Dunkelberger, P. B. Klein, A. J. Giles, J. D. Caldwell, and J. C. Owrutsky, Photoinduced tunability of the reststrahlen band in 4H-SiC, *Phys. Rev. B* **93**, 085205 (2016).

- [8] C. T. Ellis, J. G. Tischler, O. J. Glembocki, F. J. Bezares, A. J. Giles, R. Kasica, L. Shirey, J. C. Owrutsky, D. N. Chigrin, and J. D. Caldwell, Aspect-ratio driven evolution of high-order resonant modes and near-field distributions in localized surface phonon polariton nanostructures, *Sci. Rep.* **6**, 32959 (2016).
- [9] C. R. Gubbin, S. A. Maier, and S. De Liberato, Theoretical investigation of phonon polaritons in SiC micropillar resonators, *Phys. Rev. B* **95**, 035313 (2017).
- [10] A. M. Dubrovkin, B. Qiang, T. Salim, D. Nam, N. I. Zheludev, and Q. J. Wang, Resonant nanostructures for highly confined and ultra-sensitive surface phonon-polaritons, *Nat. Commun.* **11**, 1863 (2020).
- [11] C. R. Gubbin and S. De Liberato, Theory of nonlinear polaritonics: $\chi^{(2)}$ scattering on a β -SiC surface, *ACS Photonics* **4**, 1381 (2017).
- [12] I. Razzdolski, N. C. Passler, C. R. Gubbin, C. J. Winta, R. Cernansky, F. Martini, A. Politi, S. A. Maier, M. Wolf, A. Paarmann, and S. De Liberato, Second harmonic generation from strongly coupled localized and propagating phonon-polariton modes, *Phys. Rev. B* **98**, 125425 (2018).
- [13] S. Kitade, A. Yamada, I. Morichika, K. Yabana, and S. Ashihara, Nonlinear shift in phonon-polariton dispersion on a SiC surface, *ACS Photonics* **8**, 152 (2021).
- [14] T. Taubner, D. Korobkin, Y. Urzhumov, G. Shvets, and R. Hillenbrand, Near-field microscopy through a SiC superlens, *Science* **313**, 1595 (2006).
- [15] R. Kiessling, Y. Tong, A. J. Giles, S. Gewinner, W. Schölkopf, J. D. Caldwell, M. Wolf, and A. Paarmann, Surface phonon polariton resonance imaging using long-wave infrared-visible sum-frequency generation microscopy, *ACS Photonics* **6**, 3017 (2019).
- [16] T. Wang, P. Li, D. N. Chigrin, A. J. Giles, F. J. Bezares, O. J. Glembocki, J. D. Caldwell, and T. Taubner, Phonon-polaritonic bowtie nanoantennas: Controlling infrared thermal radiation at the nanoscale, *ACS Photonics* **4**, 1753 (2017).
- [17] P. Li, I. Dolado, F. J. Alfaro-Mozaz, F. Casanova, L. E. Hueso, S. Liu, J. H. Edgar, A. Y. Nikitin, S. Vélez, and R. Hillenbrand, Infrared hyperbolic metasurface based on nanostructured van der Waals materials., *Science* **359**, 892 (2018).
- [18] K. Chaudhary, M. Tamagnone, X. Yin, C. M. Spägle, S. L. Oscurato, J. Li, C. Persch, R. Li, N. A. Rubin, L. A. Jauregui, K. Watanabe, T. Taniguchi, P. Kim, M. Wuttig, J. H. Edgar, A. Ambrosio, and F. Capasso, Polariton nanophotonics using phase-change materials, *Nat. Commun.* **10**, 4487 (2019).
- [19] P. Li, X. Yang, T. W. W. Maß, J. Hanss, M. Lewin, A.-K. U. Michel, M. Wuttig, and T. Taubner, Reversible optical switching of highly confined phonon-polaritons with an ultrathin phase-change material, *Nat. Mater.* **15**, 870 EP (2016).
- [20] C. R. Gubbin, F. Martini, A. Politi, S. A. Maier, and S. De Liberato, Strong and Coherent Coupling between Localized and Propagating Phonon Polaritons, *Phys. Rev. Lett.* **116**, 246402 (2016).
- [21] N. C. Passler, C. R. Gubbin, T. G. Folland, I. Razzdolski, D. S. Katzer, D. F. Storm, M. Wolf, S. De Liberato, J. D. Caldwell, and A. Paarmann, Strong coupling of epsilon-near-zero phonon polaritons in polar dielectric heterostructures, *Nano Lett.* **18**, 4285 (2018).
- [22] C. R. Gubbin, R. Berte, M. A. Meeker, A. J. Giles, C. T. Ellis, J. G. Tischler, V. D. Wheeler, S. A. Maier, J. D. Caldwell, and S. De Liberato, Hybrid longitudinal-transverse phonon polaritons, *Nat. Commun.* **10**, 1682 (2019).
- [23] A. Bylinkin, M. Schnell, M. Autore, F. Calavalle, P. Li, J. Taboada-Gutiérrez, S. Liu, J. H. Edgar, F. Casanova, L. E. Hueso, P. Alonso-Gonzalez, A. Y. Nikitin, and R. Hillenbrand, Real-space observation of vibrational strong coupling between propagating phonon polaritons and organic molecules, *Nat. Photonics* **15**, 197 (2021).
- [24] K. Ohtani, B. Meng, M. Franckić, L. Bosco, C. Ndebeka-Bandou, M. Beck, and J. Faist, An electrically pumped phonon-polariton laser, *Sci. Adv.* **5**, eaau1632 (2019).
- [25] N. P. Kryuchkov, V. V. Brazhkin, and S. O. Yurchenko, Anticrossing of longitudinal and transverse modes in simple fluids, *J. Phys. Chem. Lett.* **10**, 4470 (2019).
- [26] C. R. Gubbin and S. De Liberato, Optical Nonlocality in Polar Dielectrics, *Phys. Rev. X* **10**, 021027 (2020).
- [27] C. R. Gubbin and S. De Liberato, Nonlocal scattering matrix description of anisotropic polar heterostructures, *Phys. Rev. B* **102**, 235301 (2020).
- [28] C. R. Gubbin and S. De Liberato, Impact of phonon nonlocality on nanogap and nanolayer polar resonators, *Phys. Rev. B* **102**, 201302(R) (2020).
- [29] C. Ciraci, R. T. Hill, J. J. Mock, Y. Urzhumov, A. I. Fernandez-Dominguez, S. A. Maier, J. B. Pendry, A. Chilkoti, and D. R. Smith, Probing the ultimate limits of plasmonic enhancement., *Science* **337**, 1072 (2012).
- [30] C. Ciraci, J. B. Pendry, and D. R. Smith, Hydrodynamic model for plasmonics: A macroscopic approach to a microscopic problem., *Chem. Phys. Chem.* **14**, 1109 (2013).
- [31] S. Rajabali, E. Cortese, M. Beck, S. De Liberato, J. Faist, and G. Scalari, Polaritonic non-locality in ultrastrong light-matter coupling, *Nat. Photonics* **15**, 690 (2021).
- [32] J. J. Hopfield, Theory of the contribution of excitons to the complex dielectric constant of crystals, *Phys. Rev.* **112**, 1555 (1958).
- [33] F. Alpeggiani and L. C. Andreani, Quantum theory of surface plasmon polaritons: Planar and spherical geometries, *Plasmonics* **9**, 965 (2014).
- [34] C. R. Gubbin, S. A. Maier, and S. De Liberato, Real-space hopfield diagonalization of inhomogeneous dispersive media, *Phys. Rev. B* **94**, 205301 (2016).
- [35] I. Carusotto and C. Ciuti, Quantum fluids of light, *Rev. Mod. Phys.* **85**, 299 (2013).
- [36] L. B. Tan, O. Cotlet, A. Bergschneider, R. Schmidt, P. Back, Y. Shimazaki, M. Kroner, and A. İmamoğlu, Interacting Polaron-Polaritons, *Phys. Rev. X* **10**, 021011 (2020).
- [37] D. K. Efimkin, E. K. Laird, J. Levinsen, M. M. Parish, and A. H. MacDonald, Electron-exciton interactions in the exciton-polaron problem, *Phys. Rev. B* **103**, 075417 (2021).
- [38] D. C. Ratchford, *et al.*, Controlling the infrared dielectric function through atomic-scale heterostructures, *ACS Nano* **13**, 6730 (2019).
- [39] R. Berte, C. R. Gubbin, V. D. Wheeler, A. J. Giles, V. Giannini, S. A. Maier, S. De Liberato, and J. D. Caldwell, Sub-nanometer thin oxide film sensing with localized surface phonon polaritons, *ACS Photonics* **5**, 2807 (2018).

- [40] J. D. Caldwell, O. J. Glembocki, Y. Francescato, N. Sharac, V. Giannini, F. J. Bezares, J. P. Long, J. C. Owrutsky, I. Vurgaftman, and J. G. Tischler, *et al.*, Low-loss, extreme subdiffraction photon confinement via silicon carbide localized surface phonon polariton resonators, *Nano Lett.* **13**, 3690 (2013).
- [41] S. A. Maier, *Plasmonics: Fundamentals and Applications* (Springer US, 2007), Chapter 2, p. 30.
- [42] I. De Leon, J. E. Sipe, and R. W. Boyd, Self-phase-modulation of surface plasmon polaritons, *Phys. Rev. A* **89**, 013855 (2014).
- [43] W. J. Moore, R. T. Holm, M. J. Yang, and J. A. Freitas, Infrared dielectric constant of cubic SiC, *J. Appl. Phys.* **78**, 7255 (1995).
- [44] A. Debernardi, C. Ulrich, K. Syassen, and M. Cardona, Raman linewidths of optical phonons in 3C-SiC under pressure: First-principles calculations and experimental results, *Phys. Rev. B* **59**, 6774 (1999).
- [45] S. Campione, I. Brener, and F. Marquier, Theory of epsilon-near-zero modes in ultrathin films, *Phys. Rev. B* **91**, 121408(R) (2015).
- [46] T. G. Folland, G. Lu, A. Bruncz, J. R. Nolan, T. Tadjer, and J. D. Caldwell, Vibrational coupling to epsilon-near-zero waveguide modes, *ACS Photonics* **7**, 614 (2020).
- [47] C. Wang, C. Qian, H. Hu, L. Shen, Z. J. Wang, H. Wang, Z. Xi, B. Zhang, H. Chen, and X. Lin, Superscattering of light in refractive-index near-zero environments, *Prog. Electromagnetics Res.* **168**, 15 (2020).
- [48] I. Liberal and N. Engheta, Manipulating thermal emission with spatially static fluctuating fields in arbitrarily shaped epsilon-near-zero bodies, *Proc. National Acad. Sci.* **115**, 2878 (2018).
- [49] A. M. Mahmoud and N. Engheta, Wave-matter interactions in epsilon-and-mu-near-zero structures, *Nat. Commun.* **5**, 5638 (2014).
- [50] N. Rivera, J. Coulter, T. Christensen, and P. Narang, Ab initio calculation of phonon polaritons in silicon carbide and boron nitride, arXiv (2018), arXiv:1809.00058.
- [51] K. Karch, P. Pavone, W. Windl, O. Schütt, and D. Strauch, Ab initio calculation of structural and lattice-dynamical properties of silicon carbide, *Phys. Rev. B* **50**, 17054 (1994).
- [52] B. Neuner III, D. Korobkin, C. Fietz, D. Carole, G. Ferro, and G. Shvets, Critically coupled surface phonon-polariton excitation in silicon carbide, *Opt. Lett.* **34**, 2667 (2009).
- [53] A. Paarmann, I. Razdolski, S. Gewinner, W. Schöllkopf, and M. Wolf, Effects of crystal anisotropy on optical phonon resonances in midinfrared second harmonic response of SiC, *Phys. Rev. B* **94**, 134312 (2016).
- [54] N. Sannodo, A. Osumi, S. Maruyama, and Y. Matsumoto, Vapor-liquid-solid-like growth of thin film SiC by nanoscale alternating deposition of SiC and NiSi₂, *Appl. Surf. Sci.* **530**, 147153 (2020).
- [55] A. J. Giles, S. Dai, I. Vurgaftman, T. Hoffman, S. Liu, L. Lindsay, C. T. Ellis, N. Assefa, I. Chatzakis, T. L. Reinecke, J. G. Tischler, M. M. Fogler, J. H. Edgar, D. N. Basov, and J. D. Caldwell, Ultralow-loss polaritons in isotopically pure boron nitride, *Nat. Mater.* **17**, 134 (2018).
- [56] C. R. Gubbin, S. De Liberato, and T. G. Folland, Perspective: Phonon polaritons for infrared optoelectronics, *J. Appl. Phys.* **131**, 030901 (2022).
- [57] C. R. Gubbin and S. De Liberato, Electrical generation of surface phonon polaritons, In preparation.